Catalysis Today 444 (2025) 115011

Contents lists available at ScienceDirect

Catalysis Today

journal homepage: www.elsevier.com/locate/cattod

Exsolution of Ni nanoparticles from $La_{0.4}Sr_{0.4}Ti_{0.8}Ni_{0.2}O_{3-\delta}$ perovskite for ethanol steam reforming

Fernando Piazzolla [a], Tamara S. Moraes [a], Stefany S. Figueiredo [a], Dryade F. de Paula [a], Emerson L. dos Santos Veiga [a], Cristiane B. Rodella [b], Fabio C. Fonseca [a,*]

[a] Nuclear and Energy Research Institute (IPEN-CNEN), São Paulo, SP 05508-000, Brazil
[b] Brazilian Synchrotron Light Laboratory (LNLS), Brazilian Center for Research in Energy and Materials (CNPEM), Campinas 6192, Brazil

ARTICLE INFO

Keywords:
Exsolution
Ethanol steam reforming
Hydrogen
Biofuels

ABSTRACT

The escalating increase in global temperatures has highlighted hydrogen (H_2) as a promising alternative clean energy carrier. Hydrogen can be derived from biofuels such as bioethanol, offering an efficient liquid carrier that addresses availability, storage, and distribution issues hindering a widespread use of H_2. This study reports on the synthesis of $La_{0.4}Sr_{0.4}Ti_{0.8}Ni_{0.2}O_{3-\delta}$ catalysts followed by the exsolution process to enhance catalytic activity for H_2 production via ethanol steam reforming (ESR) reaction. Single-phase compounds with exsolved metallic nanoparticles were successfully tested for ESR, revealing an ethanol conversion rate of 40 % and over 40 % H_2 production for the catalyst reduced at 1000 °C for 12 hours. Stability tests demonstrated the catalyst's capacity for regeneration in both water vapor and N_2. The experimental data demonstrate that exsolving metallic nanoparticles is a viable strategy for producing a stable catalyst for the ESR reaction.

1. Introduction

The use of fossil fuels for energy generation has significantly contributed to the increased emission of greenhouse gases and, consequently, accelerated global warming. Amidst this scenario, the search for alternative and environmentally friendly energy sources has intensified in recent years, with the use of hydrogen (H_2) as clean energy carrier emerging as a promising option for various applications [1–3]. Hydrogen production derived from biofuels such as bioethanol is being recognized as a clean and attractive sustainable energy source. Bioethanol is as a cost-competitive fuel produced on a large scale and widely distributed in four continents [4–6].

Bioethanol can be converted into H_2 through three main thermochemical processes: ethanol steam reforming (ESR), partial oxidation (POX), and autothermal steam reforming (OSR) [7]. ESR is receiving special attention because theoretically, for each mol of ethanol used, up to 6 moles of hydrogen can be produced (Eq. 1). To achieve this, it is important to optimize reaction conditions such as the molar ratio of water and ethanol, temperature, and residence time, as well as to select the appropriate catalyst (including support and metal) to achieve high conversion rates and selectivity for H_2 [8].

$$CH_3CH_2OH + 3\ H_2O \rightleftharpoons 6\ H_2 + 2\ CO_2 \quad (1)$$

Typically, metallic nanoparticles embedded in oxide surfaces are extensively studied catalysts for ESR. However, these catalysts face two primary deactivation processes: i) long-term stability is compromised due to carbon formation on the surface of the active metal, and ii) sintering of active phase particles occurs during reactions [9]. More recently, perovskite materials, such as strontium/titanium-based oxides, such as $LaSrTiO_3$ (LST) have emerged as promising solutions to address these deactivation challenges. They exhibit resistance to carbon formation, thermal stability under oxidizing and reducing atmospheres, and the flexibility of B-site doping [10,11]. Nevertheless, such oxides demonstrate lower catalytic activity compared to standard impregnated metallic nanoparticles. Therefore, doping the perovskite structure with transition metals, such as Ni, presents a promising strategy to enhance catalytic activity in these oxides [12-14].

To prevent the deactivation of standard catalysts, with supported impregnated metallic particles, the production of exsolved nanoparticles from an oxide matrix emerges as a promising alternative for obtaining stable metallic nanoparticles with high catalytic activity [15–17]. In exsolution, the metal is firstly incorporated into the crystal structure of the oxide matrix, forming a solid solution, and it is subsequently precipitated (exsolved) at the surface of the matrix by a thermal

* Corresponding author.
E-mail address: fabiocf@usp.br (F.C. Fonseca).

https://doi.org/10.1016/j.cattod.2024.115011
Received 3 May 2024; Received in revised form 9 August 2024; Accepted 21 August 2024
Available online 22 August 2024

reduction treatment. This process ensures a uniform and homogeneous distribution of the metal on the matrix surface [18].

Several studies report the exsolution of Ni particles in perovskites with similar compositions of LST. For instance, the utilization of strontium titanate ($La_{0.45}Sr_{0.45}Ti_{0.90}Ni_{0.10}O_{3-\delta}$) with exsolved Ni has been documented for application as an anode (electrocatalyst) in solid oxide fuel cells for H_2 production. The material was synthesized with 10 mol% of Ni by chemical route and showed promising results for ammonia decomposition and hydrogen production [19]. A similar perovskite with the general formula $La_{0.4}Ca_{0.4}Ni_xTi_{1-x}O_{3-\delta}$ (x = 0.03–0.09) was studied for the ESR reaction. Nickel was used to substitute the Ti B-site of the copmpound, synthesized by solid-state reaction. The catalytic tests showed that the sample with the highest molar concentration of Ni (x = 0.09) had the best ethanol conversion rate and higher selectivity for H_2, compared to the samples with lower Ni concentration [18]. Along with Ni nanoparticles, other monometallic exsolved active phases such as Cu [20,21], Pt [22], Rh [23], and Ru [15], and bimetallic systems like Ni-Cu [24], Ni-Pt [25], and Co-Fe(Ru) [26], have been reported for several catalytic reactions.

The objective of this study is to synthesize a novel high Ni-concentration doped LST (LSTN) using a wet synthesis method, targeting the nominal composition $La_{0.4}Sr_{0.4}Ti_{0.8}Ni_{0.2}O_{3-\delta}$. By exploring the correlation between exsolution treatment parameters, such as temperature and time, and catalytic activity for ESR reactions, this study provides a novel approach to optimize catalyst performance.

2. Experimental

2.1. Catalyst synthesis

The material with nominal composition $La_{0.4}Sr_{0.4}Ti_{0.8}Ni_{0.2}O_{3-\delta}$, named LSTN, was prepared by the Pechini method. Initially, the precursors $Ni(NO_3)_2{\cdot}6\ H_2O$ (99 %, Sigma-Aldrich), $La(NO_3)_3{\cdot}6\ H_2O$ (99.999 %, Sigma-Aldrich), $Sr(NO_3)_2$ (99.0 %, Sigma-Aldrich), and $C_{12}H_{28}O_4Ti$ (97 %, Sigma-Aldrich) were sequentially dissolved at 30-minute intervals in a solution of 100 mL of citric acid ($C_6H_8O_7$, 99.5 %, Vetec), maintaining a molar ratio of 2:1 of citric acid to the total metal ions, in a polytetrafluoroethylene (PTFE) vessel. The mixture was heated to approximately 60 °C. At this point, ethylene glycol [$(CH_2OH_2)_2$, 99 %, Sigma-Aldrich] was added to the heated solution in a 60:40 % ratio of citric acid to ethylene glycol and kept stirring for 1 hour. Then, the solution was heated in an oil bath at 180 °C until complete drying of the material.

After complete evaporation of the solvent, the material underwent thermal treatment at 250 °C for 3 hours under synthetic air (79.1 % of N_2 and 20.9 % of O_2, 99.999 % purity) to dry the formed resin. Subsequently, the material was grounded and calcined in air at a temperature of 1200 °C, with a heating ramp of 10 °C min^{-1}.

For the formation of metallic particles by exsolution, a thermal treatment was carried out in a tubular furnace using a pure H_2 atmosphere (99.9999 %), with a flow rate of approximately 10 mL min^{-1}. The heating rate was 10 °C min^{-1}, and temperatures of 750 and 1000 °C were used with different treatment times of 5 and 12 hours. These temperatures were chosen to ensure complete reduction of the nickel particles [27] and to provide sufficient energy for their precipitation on the surface of the material [28,29].

To facilitate readability, samples are labeled according to the temperature and duration of the reducing exsolution treatment. Thus, samples reduced at 750 °C for 5 hours and 12 hours are denoted as LSTN750_5 and LSTN750_12, respectively. Likewise, samples reduced at 1000 °C for 5 hours and 12 hours are denoted as LSTN1000_5 and LSTN1000_12, respectively.

2.2. Characterization of the catalysts

X-ray diffraction (XRD) analyses were carried out in the powder X-rays diffraction line of the synchrotron radiation facility at the National Synchrotron Light Laboratory (LNLS, Brazil). The wavelength 0.635639 Å was used with a Debye-Scherrer geometry for data collection at room temperature in the range of $8° \leq 2\theta \leq 35°$ with a step size of 0.01° and 1 s counting time at each step.

The microstructure and morphology of the samples were analyzed using a Zeiss Ultra 55 Field-Emission Scanning Electron Microscope (FE-SEM) with an acceleration voltage of 20 kV and a JEOL - JSM-6701 F FE-SEM with an acceleration voltage of 5 kV. The average grain diameter and nanoparticle size and number per area were estimated using ImageJ software.

Semi-quantitative compositional analysis of the samples was conducted using wavelength dispersive X-ray fluorescence (WDXRF), employing a Rigaku Supermini200 apparatus equipped with a Pd radiation source.

Specific surface area measurements were conducted using the Brunauer-Emmett-Teller (BET) method, employing a Micromeritics ASAP 2020 apparatus.

Raman spectra were recorded within the frequency range of 200 – 1200 cm^{-1} using a Horiba Jobin Yvon model XploRA-PLUS spectrometer. The spectrometer was equipped with a laser emitting at a wavelength of 532 nm and a 50x objective lens. The data acquisition and analysis were facilitated by the LabSpec6 software.

Simultaneous thermogravimetric and thermal differential analysis (TG-DTA) measurements were conducted employing a Setaram-LabSys instrument within the temperature range of 100–1000 °C. The heating rate applied was 5 °C min^{-1}, and the experiments were performed under a synthetic air flow (~50 mL min^{-1}).

2.3. Ethanol steam reforming (ESR) reaction conditions

Catalytic tests were conducted in a fixed-bed reactor using a U-shaped quartz tube with an internal diameter of 6 mm. In each experiment, to evaluate the performance of the catalyst, different weight-to-flow (W/F) ratios ((weight of catalyst)/(total gas flow rate)) were assessed: 0.02 and 0.06 g s mL^{-1}, which represent 20 mg and 60 mg of catalyst in the reactor, respectively. Preceding the experiment, an *in-situ* reducing treatment was conducted on the compound using a pure hydrogen flow (30 mL min^{-1}) at 600 °C for 1 hour to clean de surface from possible adsorbed species. Subsequently, a purge was performed with a nitrogen flow at the same temperature for 10 minutes. Finally, the reaction was conducted at 600 °C, using a reaction mixture composed of water and ethanol in a molar ratio of 3:1. The reaction mixture was introduced into the reactor through two nitrogen streams, each configured at 30 mL min^{-1}, passing separately through water and ethanol saturators. The outlet of the system was connected to a gas chromatograph (Agilent 7890 A) equipped with two chromatographic columns, a molecular sieve and a Plot U, and two detectors: the first one being a flame ionization detector (FID) and the second one a thermal conductivity detector (TCD). The ethanol conversion ($\chi_{ethanol}$) and the product distribution (S_x) were determined according to Eqs. 2 and 3:

$$\chi_{ethanol} = \frac{\left((n_{ethanol})fed \quad / (n_{ethanol})exit\right)}{n_{ethanol}} \cdot 100 \tag{2}$$

$$s_x = \frac{(n_x)produced}{(n_{total})produced} \cdot 100 \tag{3}$$

where (n_x) represents the moles of product *x* generated, while (n_{total}) denotes the total sum of moles of all products generated (excluding moles of water produced).

3. Results and discussion

The chemical composition was measured by semi-quantitative WDXRF and the results, displayed in Table 1, are in reasonable

Table 1
Elemental composition of sample LSTN determined by WDXRF analysis (oxygen balanced). Specific surface area (S_{BET}) for LSTN.

Sample	Elements (mass %)				S_{BET} ($m^2\ g^{-1}$)
	La	Sr	Ti	Ni	
Nominal	39.4	24.9	27.2	8.5	-
LSTN	39	29	22	9.8	4.3

agreement with the nominal values.

The XRD pattern of the as-prepared sample LSTN (Fig. 1) reveals single-phase compound with a cubic perovskite structure (*Pm-3 m* space group), similar to the reference phase $La_{0.4}Sr_{0.6}TiO_3$ (COD 1538294 [30]). By comparing the LSTN XRD data and the reference sample, it is possible to determine a shift of the maximum relative intensity diffraction peak to lower 2θ values (Fig. 1, right side panel). This 2θ shift indicates an expansion of the unit cell due to the incorporation of Ni [31]. The expansion of the unit cell probably occurs due to the larger size of Ni^{2+} (69 pm, coordination number, CN = 6 [32]), partially replacing the Ti^{4+} cations (60.5 pm, CN = 6 [32]). The position of the peak corresponding to the (110) plane, as shown in the enlarged panel of Fig. 1, was 13.16° for the LSTN sample and 13.15° for all the reduced samples. This indicates a shift from the standard position of 13.21°, represented by the red dotted line. There are no significant changes in the shift of the XRD peaks when varying the conditions of the reducing treatment.

Although many studies report a shrinkage of the unit cell in La-doped systems on the A site of $SrTiO_3$ [33,34], there are reports that the dominant factor influencing the expansion or contraction of the cell is the size of the cation on the B site in similar structures [35]. Additionally, the presence of oxygen vacancies can induce Coulombic repulsion between neighboring cations, causing expansion of the crystal lattice [35].

After reducing the LSTN under different conditions, the XRD data show a slight shift towards lower angles, which is likely due to a partial

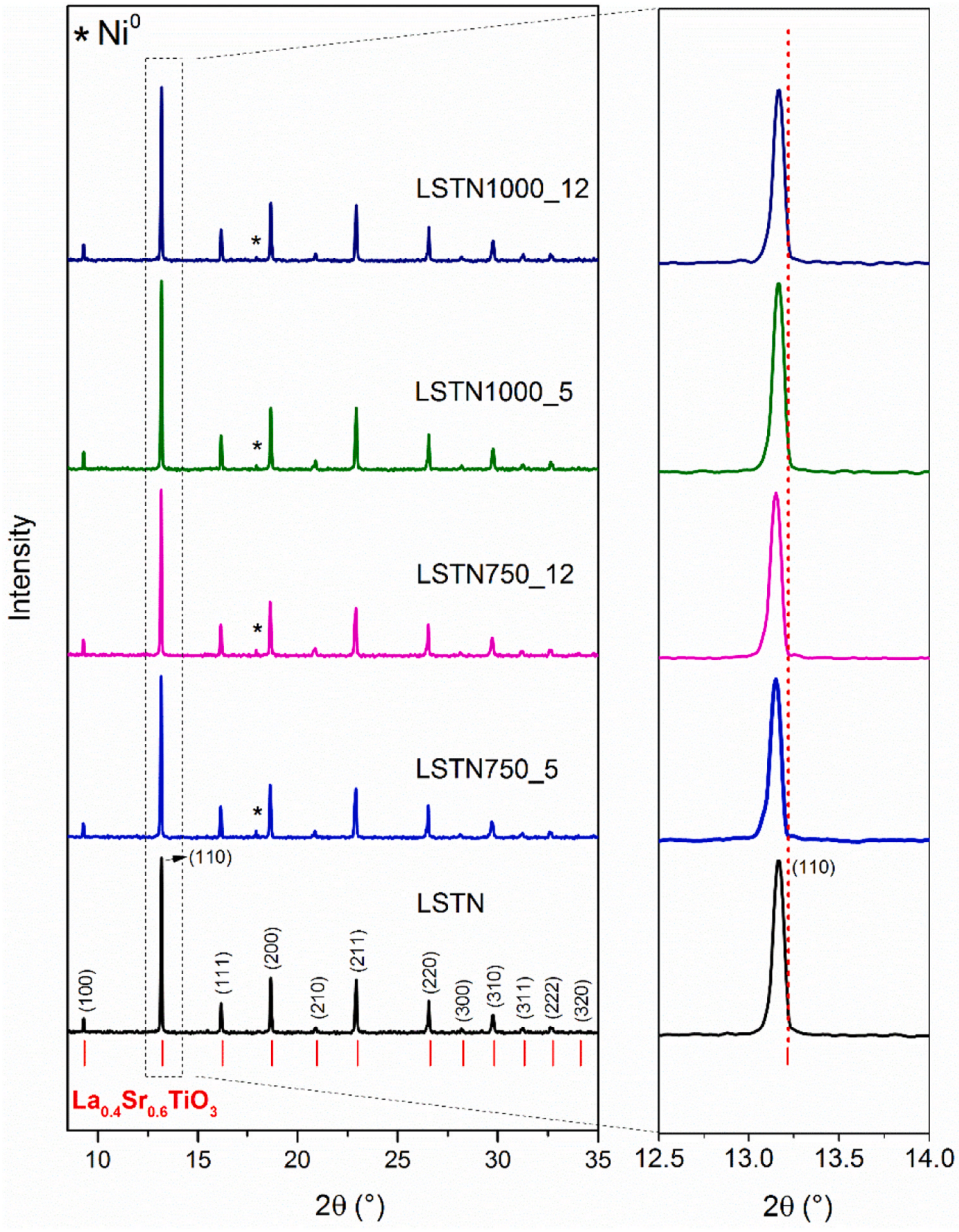

Fig. 1. X-ray diffraction patterns of the calcined (LSTN) and reduced samples after heat treatment in H_2 at different temperatures and time compared to the reference phase $La_{0.4}Sr_{0.6}TiO_3$.

reduction of Ti^{4+} to Ti^{3+} (67 pm, CN = 6 [32]) [36], leading to the formation of more oxygen vacancies and an expansion of the BO_6 octahedron, which is expected upon reduction [35]. Furthermore, there is a small peak at 2θ ~18° corresponding to Ni^0 (ICSD 37502 [37]), strongly indicating the exsolution of Ni in the reduced samples. The partial removal of Ni from the crystal structure plays a role in the observed changes of the lattice parameter of LSTN.

The micrographs obtained by FE-SEM show well-defined grains of LSTN (Fig. 2a) with typical morphology of sintered ceramics. The calculated average grain diameter was 116 ± 38 nm (Table 2). The resulting microstructure of the LSTN after calcining at 1200 °C is reflected in the relatively low specific surface area of 4.3 m^2g^{-1} determined by the BET method (Table 1).

After the reducing treatment, the microstructural features of the oxide matrix are preserved, and bright contrast spots corresponding to metallic nanoparticles are distributed over the surface of all reduced samples, as shown in Fig. 2b-e. Such nanoparticles indicate that Ni^0 was successfully exsolved onto the surface of the oxide matrix, as commonly seen in previous reports of similar LST-based compounds exsolved [19,38–40].

All samples exhibited grain growth of the oxide matrix due to the reducing thermal treatment, as depicted in the calculated average grain size presented in Table 2. There was no significant difference in the grain size of the oxide matrix when the temperature of the reducing treatment was increased from 750 °C to 1000 °C. Similarly, no notable change in grain size was detected when heat treatment time was increased from 5 hours and 12 hours.

The various conditions of the reducing treatment resulted in Ni exsolved nanoparticles with distinct characteristics, as listed in Table 2. The different temperatures used for the reducing treatment enabled the control of the metallic particle size, whereas increasing the duration of the reducing treatment promoted an increased number of metallic exsolved nanoparticles per area, calculated as the number of Ni particles in a fixed area of the samples. For samples reduced at 750 °C, the average size of exsolved nanoparticles shows no significant difference. However, there is a variation in the amount of Ni produced, with 16 ± 2 and 30 ± 3 particles per square micrometer with increasing reducing treatment time from 5 hours to 12 hours, respectively. Elevating the reducing treatment temperature to 1000 °C resulted in an increased average size of the exsolved nanoparticles, whereas with increasing time the number of exsolved nanoparticles per unit area was similar to that of the samples reduced at 750 °C. This finding is in line with the classical nucleation theory, indicating that particle formation predominantly happens at lower temperatures, while particle growth predominates at higher temperatures [28,29,41,42]. In addition, according to the literature, since exsolution in this case is induced by a secondary heat treatment at a lower temperature than the calcination temperature, no significant change or even a slight decrease in the surface area of the matrix is expected [43,44].

The formation of Ni^0 nanoparticles is particularly interesting for catalytic applications, such as the ESR reaction [45–48]. The size distribution of active metal particles and their interaction with the oxide matrix provided by the exsolution process can be decisive in controlling selectivity, catalytic activity, and resistance to carbon deposition [49].

Fig. 3 illustrates the ESR reaction at 600 °C under an H_2O/ethanol molar ratio of 3.0 using 20 mg of the reduced LSTN samples. The as-prepared material exhibited no catalytic activity for the ESR reaction (not shown), attributed to the absence of metallic particles necessary for promoting the cleavage of the C-C bond.

The LSTN750_5, LSTN750_12, and LSTN1000_5 materials displayed low ethanol conversion, with a rapid deactivation within the initial 3 hours of the catalytic test. The deactivation is attributed to carbon formation on the catalyst surface coupled with high selectivity for acetaldehyde through ethanol dehydrogenation (Fig. 3a-c). The production of H_2 using these materials ranged between 9 % and 15 %, while the quantity of CO generated was negligible. The detection of traces of ethylene suggests that ethanol dehydration is occurring, resulting in the production of water and ethylene. As the ethanol conversion was low, the catalytic tests were not repeated for these samples.

For the post-reaction catalysts LSTN750_5, LSTN750_12, and LSTN1000_5, the mass loss during thermogravimetric (TG) analysis was minimal, as shown in Fig. 4a-c. This result is expected due to the high formation of acetaldehyde, indicating that there is no breaking of the C-C bond of ethanol, and therefore a low amount of carbon is deposited in the sample. Nevertheless, the observed initial catalyst deactivation due to carbon deposition is supported by the Raman spectra (Fig. 4e), which show the two characteristic carbon bands. The first-order G band arises from the transverse and longitudinal modes of the optical phonons, while the second-order D band involves one iTO phonon and one defect. The appearance of these bands is most common for sp^2 carbon and confirms the deposition of coke on the material surface after the reaction [50,51].

Thus, for these three samples, considering the low mass loss in TG analysis and the presence of carbon detected by Raman spectroscopy, it can be concluded that the few active sites generated by the exsolution were quickly deactivated during the reaction due to coke formation. This led the reaction to produce by-products of ethanol dehydrogenation, such as acetaldehyde.

Interestingly, the LSTN1000_12 sample (Fig. 3a) showed 100 % of initial ethanol conversion with the main products H_2, CO, CO_2, and acetaldehyde. However, LSTN1000_12 catalyst showed rapid deactivation in the first hours of the reaction. The ethanol conversion stabilized at ~40 %, with significant dehydrogenation of ethanol observed, favoring an increase in the production of acetaldehyde. Moreover, there is a notable CO_2 production, suggesting a potential contribution from the water-gas shift (WGS) reaction [52].

In the case of the LSTN1200_12 sample, which exhibited higher ethanol conversion than to the other samples, carbon deposition was also observed by post-reaction TG analysis, which showed a mass loss of ~17 % between 500 °C and 700 °C, together with the appearance of a broad peak in the DTA curve, indicating the exothermic process of carbon oxidation (Fig. 4d) in this temperature range [53,54]. The Raman spectrum for this sample (Fig. 4e) confirms the characteristic D and G bands of sp^2 carbon.

Therefore, the product distribution of the catalytic test of the LSTN1000_12 samples indicates that the main reactions occurring before deactivation is the ethanol steam reforming (Eq. 4) followed by WGS reaction (Eq. 5). After deactivation, the main reactions taking place are ethanol dehydrogenation on the catalyst surface to form acetaldehyde and H_2 (Eq. 6), and ethanol dehydration forming ethylene and water (Eq. 7), followed by ethylene decomposition forming coke and H_2 (Eq. 8). These reactions of dehydrogenation and dehydration (Eqs. 6 and 7) are typical reactions occurring on oxide supports, suggesting that after deactivation, Ni no longer has activity.

$$C_2H_5OH_{(g)} + H_2O_{(v)} \rightarrow CO_{(g)} + H_{2(g)} \quad (4)$$

$$CO + H_2O \rightarrow CO_2 + H_2 \quad (5)$$

$$C_2H_5OH \rightarrow C_2H_4O + H_2 \quad (6)$$

$$C_2H_5OH \rightarrow C_2H_{4(g)} + H_2O \quad (7)$$

$$C_2H_{4(g)} \rightarrow 2\,C_{(s)} + 2\,H_{2(g)} \quad (8)$$

The enhanced catalytic activity of LSTN1000_12 can be attributed to the reducing treatment parameters. A more intense reducing treatment, like that applied to sample LSTN1000_12, was necessary to promote a higher amount of Ni^0 nanoparticles on the surface of the oxide (Table 2).

To evaluate the influence of the W/F ratio, as well as the stability and regeneration of the material, ESR tests were repeated using the LSTN1000_12 sample with a mass of 60 mg (0.060 g s mL^{-1}). This sample was selected because it exhibited higher activity ethanol conversion rate compared to the others. The results, shown in Fig. 5a,

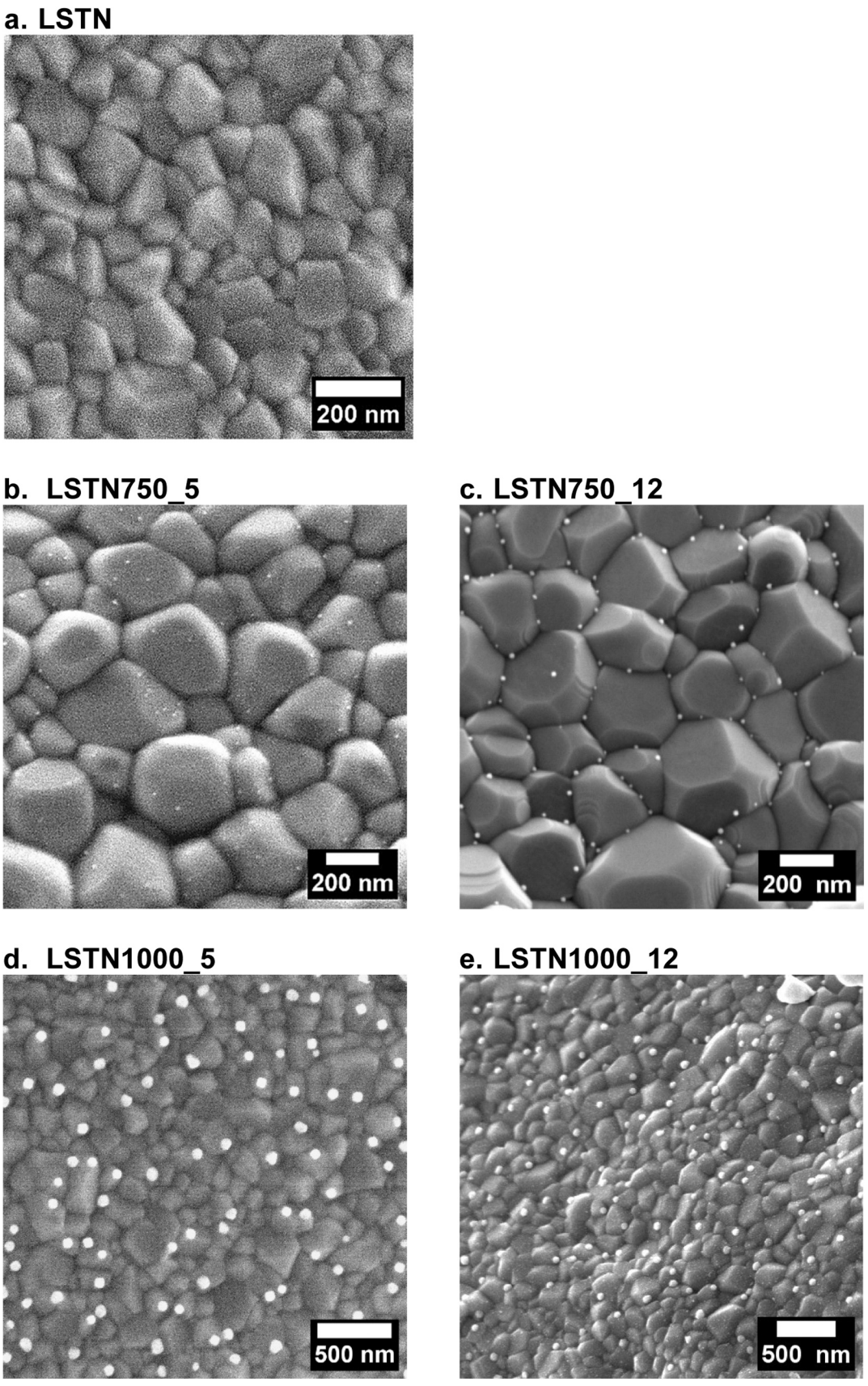

Fig. 2. FE-SEM micrographs of the as-prepared and reduced samples at different temperatures and times.

Table 2
Influence of temperature and time of reducing heat treatment on oxide matrix grain size, and on the size and number per unit area of Ni^0 exsolved particles.

Sample	Exsolution condition T (°C)/t(h)	Average oxide matrix grain size (nm)	Average Ni^0 particle size (nm)	Average number of Ni^0 particles per area (particles/ μm^2)
LSTN	-	116 ± 38	-	-
LSTN750_5	750 / 5	243 ± 84	19 ± 5	16 ± 2
LSTN750_12	750 / 12	262 ± 63	17 ± 5	30 ± 3
LSTN1000_5	1000 / 5	260 ± 79	48 ± 6	18 ± 2
LSTN1000_12	1000 / 12	272 ± 65	43 ± 4	29 ± 2

indicate that following an initial deactivation attributed to coke deposition, ethanol conversion remained nearly constant at ~40 % over the initial 20-hour test period. Such result is similar to that obtained with 0.020 g s mL^{-1} (Fig. 3d) suggesting that ethanol conversion was practically unaffected by the change in the W/F ratio. However, with an increased W/F ratio, H_2 production increased to ~46 %, while acetaldehyde production decreased to ~34 %, compared to the results shown in Fig. 3d. Moreover, CO production increased to around 10 %, indicating an enhancement in the ESR reaction (Eq. 4). These findings suggest that there are more active Ni sites available for the catalytic reaction when using a higher amount of catalyst.

To investigate the deactivation mechanism and the robustness of the exsolved LSTN catalyst, after the initial 20 hours of reaction the catalyst underwent an *in-situ* thermal treatment with water vapor at 600 °C. Such treatment was carried out to investigate whether is possible to restore the initial activity of the catalyst. After two hours under steam, ESR reaction was restarted, and similarly to the first reaction period, there was a rapid deactivation of the catalyst, stabilizing thereafter at ~50 % ethanol conversion, slightly higher than the initial conversion. Both the H_2 production was improved by 5 %, and acetaldehyde production

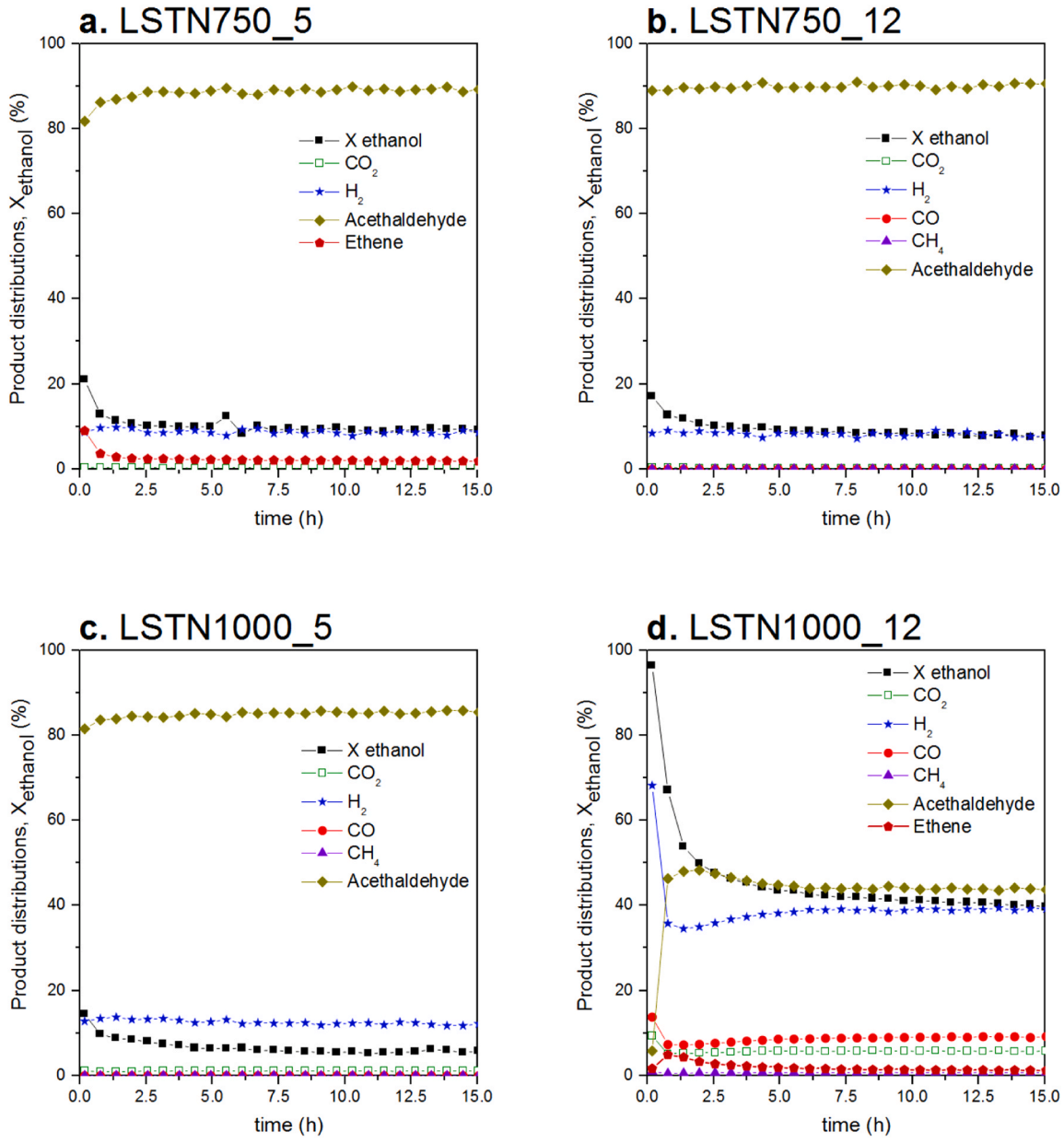

Fig. 3. Ethanol conversion and product distributions during a 15-hour reaction at 600 °C under H_2O/ethanol molar ratio = 3.0 over the reduced samples: (a) LSTN750_5, (b) LSTN750_12, (c) LSTN1000_5, and (d) LSTN1000_12 (Mass of catalyst = 20 mg and W/F ratio = 0.020 g s mL^{-1}).

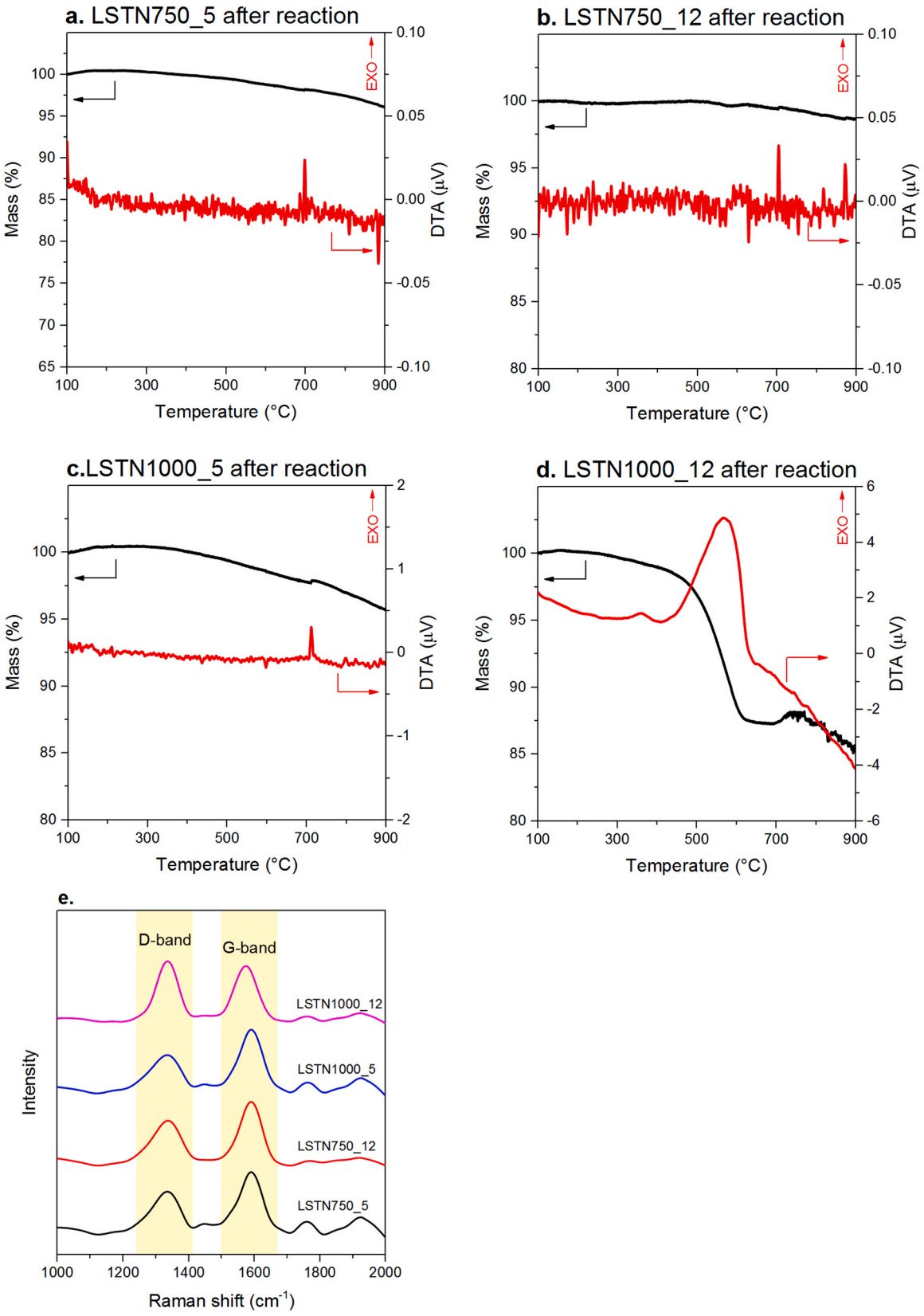

Fig. 4. (a-d) Thermogravimetric analysis (black) and differential thermal analysis (red) curves and (e) Raman spectra for all spent catalyst after ESR reaction.

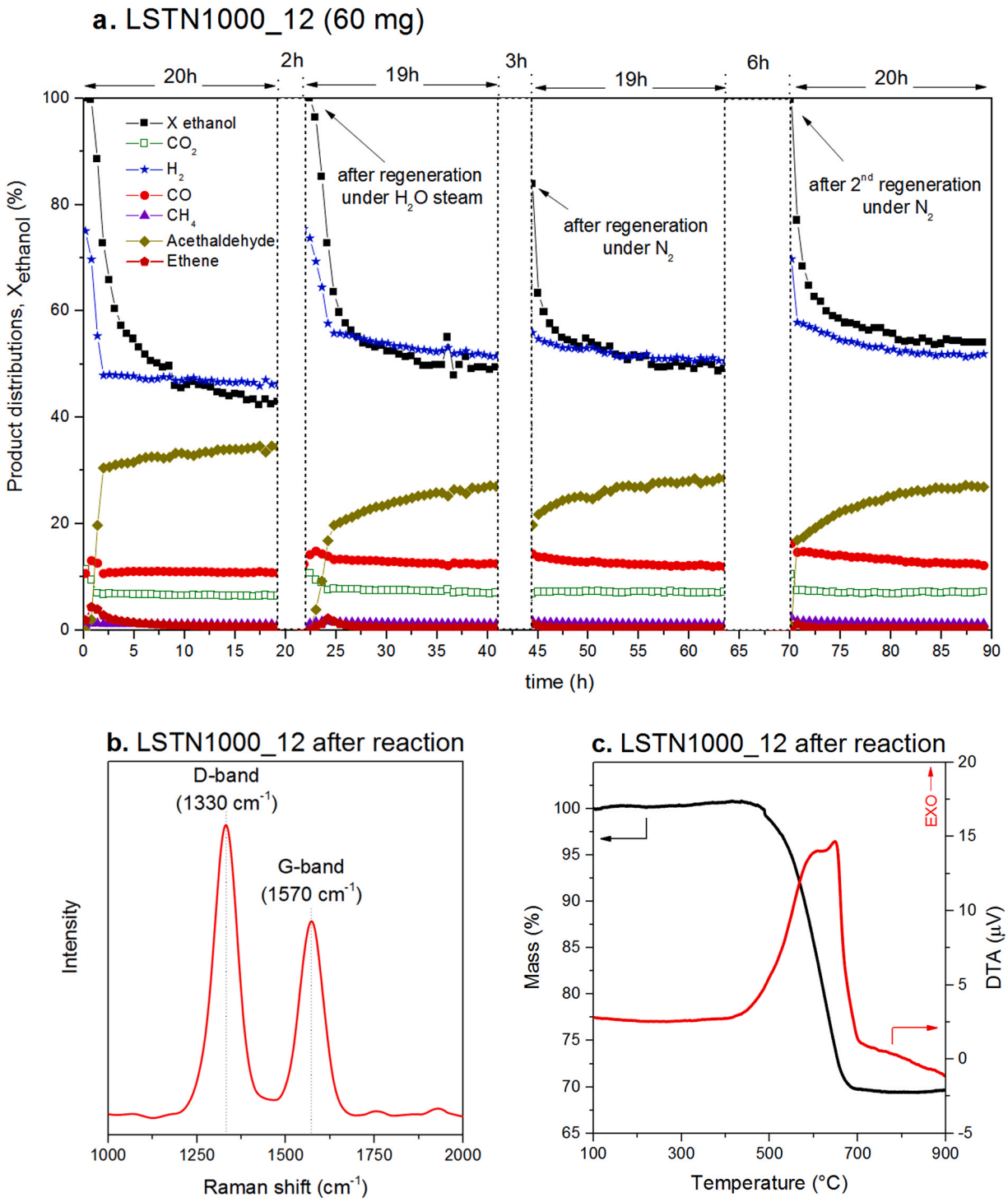

Fig. 5. (a) Ethanol conversion and product distributions during an 89-hour reaction at 600 °C under H_2O/ethanol molar ratio = 3.0 over the LSTN1000_12 sample (Mass of catalyst = 60 mg and W/F ratio = 0.060 g s mL^{-1}). (b) Raman spectra and (c) thermogravimetric analysis of LSTN1000_12 after the stability and recovery test.

decreased 7 % compared to the first reaction period. This result indicates that the catalyst can be rapidly restored under steam, as water promotes the oxidation of the carbon species deposited on the catalyst surface during the reaction.

After additional 19 hours of ESR reaction, the inlet flow of ethanol and steam was interrupted and only N_2 was delivered to the reaction chamber to verify if catalyst recovery could be achieved in an inert atmosphere. After 3 hours in N_2, the ESR reaction was restarted, but the catalyst showed a lower ethanol conversion (83 %) than the initial one. This partial recovery of the catalytic activity can be explained by the presence of oxidizing species adsorbed on the catalyst surface, such as CO_2 [55,56], for example, in addition to the presence of oxygen from the perovskite lattice [57,58], which partially eliminate the coke deposited on the catalyst surface.

To achieve an ethanol conversion comparable to the initial level using N_2 for catalyst regeneration, an extended recovery treatment was necessary. This is evident in the final reaction step depicted in Fig. 5a, in which a 6-hour heat treatment under N_2 restored the initial catalyst

activity to 100 % ethanol conversion. The product distribution observed after each stage of the reaction demonstrate a good catalyst stability after several regeneration cycles.

In the regeneration and long-term stability, coke is the main deactivation mechanism to explain the decrease in ethanol conversion in the first hours of the reaction for the LSTN1000_12 sample. As can be seen in Fig. 5b, two bands related to carbon can be observed in the Raman spectrum, one at 1330 cm^{-1} and another at 1570 cm^{-1}, associated with the second-order D band and the first-order G band, respectively.

The bands related to coke deposition obtained by Raman analysis are corroborated by the TG profiles of the catalyst recovered after the final reaction period (Fig. 5c), showing a significant mass loss (~30 %) in the temperature range between 450 – 660 °C. Such mas loss corresponds to the decomposition temperature of sp^2 carbon species [59] deposited in the surface of the catalyst, through an exothermic oxidation process, as seen in the DTA curve. The carbon deposition rate estimated using the TG curves was 1.47 $mg_{carbon}\ g_{catalyst}^{-1}\ h^{-1}$ at 600 °C.

4. Conclusions

In this study, successful Ni exsolution from the compound $La_{0.4}Sr_{0.4}Ti_{0.8}Ni_{0.2}O_{3-\delta}$ was demonstrated. The synchrotron XRD data revealed single-phase material upon calcination and a distinct peak corresponding to Ni^0 after applying different reducing treatments to the sample. The exsolution was further supported by FE-SEM micrographs, showing the Ni^0 nanoparticles in all reduced samples. Additionally, an increase in temperature and duration of the reducing treatment resulted in grain growth of the oxide matrix, increased number of exsolved particles per area, and higher average size of the Ni^0 exsolved nanoparticles.

Catalytic activity for ethanol steam reforming was achieved in samples with exsolved Ni^0. The product distribution of the ethanol steam reforming (ESR) reaction revealed that the sample subjected to a reducing treatment at 1000 °C for 12 hours (LSTN1000_12), exhibited higher ethanol conversion (40 %). This suggests that in samples calcined at 1200 °C, a high-temperature reducing treatment is necessary for the generation of a greater population of metallic nanoparticles with sufficient Ni fraction to promote the cleavage of the C-C bond during the ESR reaction.

For the active sample, stability and regeneration tests were carried out. By increasing the weight-to-flow ratio, a similar conversion was observed, albeit with significant changes in product distribution, such as the increase in H_2, CO, and CO_2 production. It was demonstrated that the exsolved catalyst can be regenerated in water vapor in ~2 hours, and more slowly (~6 hours) in N_2. In all catalytic tests performed, there was a decrease in ethanol conversion in the initial hours of the reaction due to coke deposition on the catalyst surface. Steam oxidizes coke, promoting rapid recovery of the catalyst, while when using N_2, a longer recovery time is necessary because the coke is possibly oxidized by species adsorbed on the catalyst surface and by the oxygen present in the perovskite lattice. After the initial reduction in ethanol conversion, both the conversion and the product distribution remain stable for at least 20 hours. The formation of coke was confirmed by Raman spectroscopy.

Thus, utilizing the exsolution strategy for the formation of metallic Ni nanoparticles in an oxide matrix, a stable catalyst was obtained. This initial study presents a promising material for ethanol steam reforming reaction, which can be further optimized for higher ethanol conversion.

The synthesis of nanoparticles by the exsolution process is promising because the metal nanoparticles uniquely embed themselves into the oxide surface, enhancing the cohesion and interaction between the metal and the support. Consequently, active and stable catalysts can be formed by exsolution [60–62].

CRediT authorship contribution statement

Fernando Piazzolla: Writing – original draft, Methodology, Investigation, Formal analysis, Conceptualization. **Tamara Siqueira Moraes:** Writing – review & editing, Methodology, Investigation, Formal analysis, Conceptualization. **Dryade Ferreira de Paula:** Writing – review & editing, Methodology, Investigation, Formal analysis, Conceptualization. **Emerson Veiga:** Writing – original draft, Methodology, Investigation, Formal analysis, Conceptualization. **Cristiane Rodella:** Writing – review & editing, Resources, Methodology, Investigation, Formal analysis, Conceptualization. **Fabio Coral Fonseca:** Supervision, Resources, Project administration, Methodology, Investigation, Formal analysis, Conceptualization. **Stefany Figueiredo:** Writing – review & editing, Methodology, Investigation, Formal analysis, Conceptualization.

Declaration of Competing Interest

The authors declare that they have no known competing financial interests or personal relationships that could have appeared to influence the work reported in this paper.

Data Availability

Data will be made available on request.

Acknowledgements

The authors would like to acknowledge the support of the Comissão Nacional de Energia Nuclear (IPEN-CNEN) and the Brazilian agencies FAPESP grant n^{os} 2018/19251–7, 2019/15110–2, Finep grant n° 01.18.0073.00, CNPq Sis-H_2 407967/2022–2, and Fundep-Rota 2030 grant n° 27192*34. This work was supported by Institut Carnot Energies du Futur and by the Centre of Excellence of Multifunctional Architectured Materials "CEMAM" including the kind assistance of Frederic Charlot (CMTC - Grenoble INP) and Dr. M. C. Steil (LEPMI - Grenoble INP, UGA) with scanning electron microscopy analyses. We also thank LNLS in Brazil for the X-ray measurements. FCF is a CNPq fellow.

References

[1] P. Nikolaidis, A. Poullikkas, A comparative overview of hydrogen production processes, Renew. Sustain. Energy Rev. 67 (2017) 597–611, https://doi.org/10.1016/j.rser.2016.09.044.
[2] Z.P. Cano, D. Banham, S. Ye, A. Hintennach, J. Lu, M. Fowler, Z. Chen, Batteries and fuel cells for emerging electric vehicle markets, Nat. Energy 3 (2018) 279–289, https://doi.org/10.1038/s41560-018-0108-1.
[3] I. Staffell, D. Scamman, A. Velazquez Abad, P. Balcombe, P.E. Dodds, P. Ekins, N. Shah, K.R. Ward, The role of hydrogen and fuel cells in the global energy system, Energy Environ. Sci. 12 (2019) 463–491, https://doi.org/10.1039/C8EE01157E.
[4] B. Koul, M. Yakoob, M.P. Shah, Agricultural waste management strategies for environmental sustainability, Environ. Res. 206 (2022) 112285, https://doi.org/10.1016/j.envres.2021.112285.
[5] M.V. Rodionova, R.S. Poudyal, I. Tiwari, R.A. Voloshin, S.K. Zharmukhamedov, H. G. Nam, B.K. Zayadan, B.D. Bruce, H.J.M. Hou, S.I. Allakhverdiev, Biofuel production: challenges and opportunities, Int. J. Hydrog. Energy 42 (2017) 8450–8461, https://doi.org/10.1016/j.ijhydene.2016.11.125.
[6] D. Kumari, R. Singh, Pretreatment of lignocellulosic wastes for biofuel production: a critical review, Renew. Sustain. Energy Rev. 90 (2018) 877–891, https://doi.org/10.1016/j.rser.2018.03.111.
[7] W. Cai, F. Wang, E. Zhan, A. Vanveen, C. Mirodatos, W. Shen, Hydrogen production from ethanol over Ir/CeO_2 catalysts: a comparative study of steam reforming, partial oxidation and oxidative steam reforming, J. Catal. 257 (2008) 96–107, https://doi.org/10.1016/j.jcat.2008.04.009.
[8] L.V. Mattos, G. Jacobs, B.H. Davis, F.B. Noronha, Production of hydrogen from ethanol: review of reaction mechanism and catalyst deactivation, Chem. Rev. 112 (2012) 4094–4123, https://doi.org/10.1021/cr2000114.
[9] T.S. Moraes, V.S. Bergamaschi, J.C. Ferreira, E.V. Spinacé, Preparation and characterization of high-performance Ni-based core–shell catalyst for ethanol steam reforming, J. Mater. Sci. 57 (2022) 5384–5395, https://doi.org/10.1007/s10853-022-06969-4.
[10] S. Lou, X. Meng, N. Liu, L. Shi, A-site defects boosted exsolution on $(La_{0.5}Ca_{0.5})_{(1-\alpha)}Ni_{0.06}Ti_{0.94}O_{3-\delta}$ for ethanol steam reforming, Chem. Eng. J. 476 (2023) 146145, https://doi.org/10.1016/j.cej.2023.146145.
[11] S. He, M. Li, J. Hui, X. Yue, In-situ construction of ceria-metal/titanate heterostructure with controllable architectures for efficient fuel electrochemical

conversion, Appl. Catal. B Environ. 298 (2021) 120588, https://doi.org/10.1016/j.apcatb.2021.120588.
[12] Y. Deng, S. Li, L. Appels, H. Zhang, N. Sweygers, J. Baeyens, R. Dewil, Steam reforming of ethanol by non-noble metal catalysts, Renew. Sustain. Energy Rev. 175 (2023) 113184, https://doi.org/10.1016/j.rser.2023.113184.
[13] A.A.A. da Silva, M.C. Steil, F.N. Tabuti, R.C. Rabelo-Neto, F.B. Noronha, L. V. Mattos, F.C. Fonseca, The role of the ceria dopant on Ni / doped-ceria anodic layer cermets for direct ethanol solid oxide fuel cell, Int. J. Hydrogen Energy 46 (2021) 4309–4328. https://doi.org/10.1016/j.ijhydene.2020.10.155.
[14] M. Machado, L.N. Rodrigues, V.B. Vilela, T.S. Moraes, A.S. Ferlauto, F.C. Fonseca, Shape Control of Ceria Catalytic Supports for Enhanced Ethanol Reforming in Solid Oxide Fuel Cells, ACS Appl. Energy Mater. 7 (2024) 1766–1776. https://doi.org/10.1021/acsaem.3c02757.
[15] A.J. Carrillo, L. Navarrete, M. Laqdiem, M. Balaguer, J.M. Serra, Boosting methane partial oxidation on ceria through exsolution of robust Ru nanoparticles, Mater. Adv. 2 (2021) 2924–2934, https://doi.org/10.1039/D1MA00044F.
[16] M. Machado, F. Tabuti, F. Piazzolla, T. Moraes, R. Abe, R.M. Guimarães, Y. Miura, Y. Fukuyama, F.C. Fonseca, Steam reforming catalytic layer on anode-supported and metal-supported solid oxide fuel cells for direct ethanol operation, ECS Trans. 111 (2023) 301–311, https://doi.org/10.1149/11106.0301ecst.
[17] N.K. Monteiro, F.B. Noronha, L.O.O. da Costa, M. Linardi, F.C. Fonseca, A direct ethanol anode for solid oxide fuel cell based on a chromite-manganite with catalytic ruthenium nanoparticles, Int. J. Hydrog. Energy 37 (2012) 9816–9829, https://doi.org/10.1016/j.ijhydene.2012.03.157.
[18] S. Lou, X. Meng, N. Liu, L. Shi, A-site deficient titanate perovskite surface with exsolved nickel nanoparticles for ethanol steam reforming, Chem. Eng. Sci. 274 (2023) 118690, https://doi.org/10.1016/j.ces.2023.118690.
[19] J. Cavazzani, E. Squizzato, E. Brusamarello, A. Glisenti, Exsolution in Ni-doped lanthanum strontium titanate: a perovskite-based material for anode application in ammonia-fed solid oxide fuel cell, Int. J. Hydrog. Energy 47 (2022) 13921–13932, https://doi.org/10.1016/j.ijhydene.2022.02.133.
[20] T. Berger, H. Drexler, T. Ruh, L. Lindenthal, F. Schrenk, J. Bock, R. Rameshan, K. Föttinger, J. Irrgeher, C. Rameshan, Cu-doped perovskite-type oxides: a structural deep dive and examination of their exsolution behaviour influenced by B-site doping, Catal. Today 437 (2024) 114787, https://doi.org/10.1016/j.cattod.2024.114787.
[21] Z. Zhu, J. Zhou, Q. Li, Z. Liu, Q. Deng, Z. Zhou, C. Li, L. Fu, J. Zhou, H. Li, Q. Zhang, K. Wu, Preparation of heterostructured Cu-CeO_2/$SrTiO_3$ catalysts by rapid plasma exsolution for photothermal reverse water gas shift reaction, J. CO_2 Util. 80 (2024) 102665, https://doi.org/10.1016/j.jcou.2023.102665.
[22] G. Wang, Z. Li, Y. Gai, Z. Xu, W. Kang, Z. Li, H. Wang, K. Li, In situ exsolution of Pt nanoparticles on low Pt-substituted A-site deficient perovskite for efficient CO oxidation, Appl. Surf. Sci. 664 (2024) 160264, https://doi.org/10.1016/j.apsusc.2024.160264.
[23] M.J. Mekkering, J. Biemolt, J. de Graaf, Y.-A. Lin, N.P. van Leest, A. Troglia, R. Bliem, B. de Bruin, G. Rothenberg, N. Yan, Dry reforming of methane over single-atom Rh/Al_2O_3 catalysts prepared by exsolution, Catal. Sci. Technol. 13 (2023) 2255–2260, https://doi.org/10.1039/D2CY02126A.
[24] X. Gao, L. Ye, K. Xie, In-situ exsolved Ni-Cu alloy nanoparticles for optimization of perovskite electrodes in solid oxide electrolysis cell, Fuel 371 (2024) 131959, https://doi.org/10.1016/j.fuel.2024.131959.
[25] M. Xu, Y. Jeon, A. Naden, H. Kim, G. Kerherve, D.J. Payne, Y. Shul, J.T.S. Irvine, Synergistic growth of nickel and platinum nanoparticles via exsolution and surface reaction, Nat. Commun. 15 (2024) 4007, https://doi.org/10.1038/s41467-024-48455-2.
[26] Y. Liang, Y. Cui, Y. Chao, N. Han, J. Sunarso, P. Liang, X. He, C. Zhang, S. Liu, Exsolution of CoFe(Ru) nanoparticles in Ru-doped $(La_{0.8}Sr_{0.2})_{0.9}Co_{0.1}Fe_{0.8}Ru_{0.1}O_{3-\delta}$ for efficient oxygen evolution reaction, Nano Res. 15 (2022) 6977–6986, https://doi.org/10.1007/s12274-022-4328-0.
[27] W. Chu, W. Yang, L. Lin, Selective oxidation of methane to syngas over NiO/barium hexaaluminate, Catal. Lett. 74 (2001) 139–144, https://doi.org/10.1023/A:1016622301743.
[28] Y. Gao, D. Chen, M. Saccoccio, Z. Lu, F. Ciucci, From material design to mechanism study: nanoscale Ni exsolution on a highly active A-site deficient anode material for solid oxide fuel cells, Nano Energy 27 (2016) 499–508, https://doi.org/10.1016/j.nanoen.2016.07.013.
[29] D. Neagu, G. Tsekouras, D.N. Miller, H. Ménard, J.T.S. Irvine, In situ growth of nanoparticles through control of non-stoichiometry, Nat. Chem. 5 (2013) 916–923, https://doi.org/10.1038/nchem.1773.
[30] S.A. Howard, J.K. Yau, H.U. Anderson, Structural characteristics of $Sr_{1-x}La_xTi_{3+\delta}$ as a function of oxygen partial pressure at 1400 °C, J. Appl. Phys. 65 (1989) 1492–1498, https://doi.org/10.1063/1.342963.
[31] B. Cantor, Bragg's Law. Equations Mater, Oxford University Press, 2020, pp. 24–44, https://doi.org/10.1093/oso/9780198851875.003.0002.
[32] R.D. Shannon, Revised effective ionic radii and systematic studies of interatomic distances in halides and chalcogenides, Acta Crystallogr. Sect. A 32 (1976) 751–767, https://doi.org/10.1107/S0567739476001551.
[33] P. Nunocha, M. Kaewpanha, T. Bongkarn, A. Phuruangrat, T. Suriwong, A new route to synthesizing La-doped $SrTiO_3$ nanoparticles using the sol-gel auto combustion method and their characterization and photocatalytic application, Mater. Sci. Semicond. Process. 134 (2021) 106001, https://doi.org/10.1016/j.mssp.2021.106001.
[34] K. Park, J.S. Son, S.I. Woo, K. Shin, M.-W. Oh, S.-D. Park, T. Hyeon, Colloidal synthesis and thermoelectric properties of La-doped $SrTiO_3$ nanoparticles, J. Mater. Chem. A 2 (2014) 4217, https://doi.org/10.1039/c3ta14699e.
[35] S. Miyoshi, J.-O. Hong, K. Yashiro, A. Kaimai, Y. Nigara, K. Kawamura, T. Kawada, J. Mizusaki, Lattice expansion upon reduction of perovskite-type $LaMnO_3$ with oxygen-deficit nonstoichiometry, Solid State Ion. 161 (2003) 209–217, https://doi.org/10.1016/S0167-2738(03)00281-9.
[36] C.D. Savaniu, J. Irvine, Intermediate Temperature SOFC anode component based on A-site deficient La-doped $SrTiO_3$, ECS Trans. 25 (2009) 2213–2222, https://doi.org/10.1149/1.3205771.
[37] J.O. Conway, T.J. Prior, Interstitial nitrides revisited – a simple synthesis of M-Mo_3N (M = Fe, Co, Ni), J. Alloy. Compd. 774 (2019) 69–74, https://doi.org/10.1016/j.jallcom.2018.09.307.
[38] L. W. O'Leary, J.L.M. Giordano, Rupp, Tuning reduction conditions to understand and control Ni exsolution from $Sr_{0.8}La_{0.1}Ca_{0.1}Ti_{0.94}Ni_{0.06}O_{3-\delta}$, J. Mater. Chem. A 11 (2023) 21429–21442, https://doi.org/10.1039/D3TA04817A.
[39] J. Yang, J. Zhou, Z. Liu, Y. Sun, C. Yin, K. Wang, R. Li, Z. Zhou, K. Wu, Exploring heterogeneous phases in highly A-site-deficient titanate with Ni exsolution, J. Power Sources 580 (2023) 233369, https://doi.org/10.1016/j.jpowsour.2023.233369.
[40] H. Kim, R. Mane, K. Han, H. Kim, C. Lee, Y. Jeon, In situ control of the eluted Ni nanoparticles from highly doped perovskite for effective methane dry reforming, Nanomaterials 12 (2022) 3325, https://doi.org/10.3390/nano12193325.
[41] S.-K. Otto, K. Kousi, D. Neagu, L. Bekris, J. Janek, I.S. Metcalfe, Exsolved nickel nanoparticles acting as oxygen storage reservoirs and active sites for redox CH_4 conversion, ACS Appl. Energy Mater. 2 (2019) 7288–7298, https://doi.org/10.1021/acsaem.9b01267.
[42] W.T. Wallace, B.K. Min, D.W. Goodman, The nucleation, growth, and stability of oxide-supported metal clusters, Top. Catal. 34 (2005) 17–30, https://doi.org/10.1007/s11244-005-3786-4.
[43] X. Xiong, J. Yu, X. Huang, D. Zou, Y. Song, M. Xu, R. Ran, W. Wang, W. Zhou, Z. Shao, Slightly ruthenium doping enables better alloy nanoparticle exsolution of perovskite anode for high-performance direct-ammonia solid oxide fuel cells, J. Mater. Sci. Technol. 125 (2022) 51–58, https://doi.org/10.1016/j.jmst.2022.02.031.
[44] F.N. Agüero, A.M. Beltrán, M.A. Fernández, L.E. Cadús, Surface nickel particles generated by exsolution from a perovskite structure, J. Solid State Chem. 273 (2019) 75–80, https://doi.org/10.1016/j.jssc.2019.02.036.
[45] D. Zanchet, J.B.O. Santos, S. Damyanova, J.M.R. Gallo, J.M.C. Bueno, Toward understanding metal-catalyzed ethanol reforming, ACS Catal. 5 (2015) 3841–3863, https://doi.org/10.1021/cs5020755.
[46] Y.C. Sharma, A. Kumar, R. Prasad, S.N. Upadhyay, Ethanol steam reforming for hydrogen production: Latest and effective catalyst modification strategies to minimize carbonaceous deactivation, Renew. Sustain. Energy Rev. 74 (2017) 89–103, https://doi.org/10.1016/j.rser.2017.02.049.
[47] J.L. Contreras, J. Salmones, J.A. Colín-Luna, L. Nuño, B. Quintana, I. Córdova, B. Zeifert, C. Tapia, G.A. Fuentes, Catalysts for H 2 production using the ethanol steam reforming (a review), Int. J. Hydrog. Energy 39 (2014) 18835–18853, https://doi.org/10.1016/j.ijhydene.2014.08.072.
[48] J.H. Song, S.J. Han, I.K. Song, Hydrogen production by steam reforming of ethanol over mesoporous Ni–Al_2O_3–ZrO_2 Catalysts, Catal. Surv. Asia 21 (2017) 114–129, https://doi.org/10.1007/s10563-017-9230-5.
[49] S. Ogo, Y. Sekine, Recent progress in ethanol steam reforming using non-noble transition metal catalysts: a review, Fuel Process. Technol. 199 (2020) 106238, https://doi.org/10.1016/j.fuproc.2019.106238.
[50] Z. Li, L. Deng, I.A. Kinloch, R.J. Young, Raman spectroscopy of carbon materials and their composites: graphene, nanotubes and fibres, Prog. Mater. Sci. 135 (2023) 101089, https://doi.org/10.1016/j.pmatsci.2023.101089.
[51] A.C. Ferrari, J.C. Meyer, V. Scardaci, C. Casiraghi, M. Lazzeri, F. Mauri, S. Piscanec, D. Jiang, K.S. Novoselov, S. Roth, A.K. Geim, Raman spectrum of graphene and graphene layers, Phys. Rev. Lett. 97 (2006) 187401, https://doi.org/10.1103/PhysRevLett.97.187401.
[52] C.-C. Chen, H.-H. Tseng, Y.-L. Lin, W.-H. Chen, Hydrogen production and carbon dioxide enrichment from ethanol steam reforming followed by water gas shift reaction, J. Clean. Prod. 162 (2017) 1430–1441, https://doi.org/10.1016/j.jclepro.2017.06.149.
[53] M.G.S. Bernd, S.R. Bragança, N. Heck, L.C.P. da, S. Filho, Synthesis of carbon nanostructures by the pyrolysis of wood sawdust in a tubular reactor, J. Mater. Res. Technol. 6 (2017) 171–177, https://doi.org/10.1016/j.jmrt.2016.11.003.
[54] F. Yu, H. Wang, Y. Bai, J. Yang, Preparation and characterization of porous Si3N4 ceramics prepared by compression molding and slip casting methods, Bull. Mater. Sci. 33 (2010) 619–624, https://doi.org/10.1007/s12034-010-0094-9.
[55] J. Guo, J. Zhang, G. Wang, W. Geng, C. Zheng, Y. Chai, Characteristic and kinetics of oxidation of coke by CO_2 based on isothermal method. 6th Int. Symp. High-Temperature Metall. Process., Springer International Publishing, Cham, 2015, pp. 619–626, https://doi.org/10.1007/978-3-319-48217-0_79.
[56] M. Wang, G. Wei, R. Zhu, K. Dong, Effect of CO_2-O_2 oxidizing atmospheres on the combustion characteristics of metallurgical coke and anthracite, J. CO_2 Util. 52 (2021) 101665, https://doi.org/10.1016/j.jcou.2021.101665.
[57] A. Shahnazi, S. Firoozi, Mesoporous $LaNi_{1-x}Mn_xO_3$ perovskite with enhanced catalytic performance and coke resistance synthesized via glycine-assisted spray pyrolysis for methane dry reforming, Mol. Catal. 547 (2023) 113320, https://doi.org/10.1016/j.mcat.2023.113320.
[58] Y. Ding, X. Ma, Y. Tang, X. Chen, Effect of lattice oxygen in nickel-based catalysts with different support on coke resistance of filamentous coke in CO_2 reforming of tar, Energy Sources, Part A Recover Util. Environ. Eff. (2022) 1–14, https://doi.org/10.1080/15567036.2022.2040658.

[59] A.G. Bannov, M.V. Popov, P.B. Kurmashov, Thermal analysis of carbon nanomaterials: advantages and problems of interpretation, J. Therm. Anal. Calorim. 142 (2020) 349–370, https://doi.org/10.1007/s10973-020-09647-2.
[60] X. Sun, H. Chen, Y. Yin, M.T. Curnan, J.W. Han, Y. Chen, Z. Ma, Progress of exsolved metal nanoparticles on oxides as high performance (electro)catalysts for the conversion of small molecules, Small 17 (2021), https://doi.org/10.1002/smll.202005383.
[61] K. Kousi, C. Tang, I.S. Metcalfe, D. Neagu, Emergence and future of exsolved materials, Small 17 (2021), https://doi.org/10.1002/smll.202006479.
[62] O. Kwon, S. Joo, S. Choi, S. Sengodan, G. Kim, Review on exsolution and its driving forces in perovskites, J. Phys. Energy 2 (2020) 032001, https://doi.org/10.1088/2515-7655/ab8c1f.